

Stringent axion constraints with Event Horizon Telescope polarimetric measurements of M87*

Yifan Chen¹, Yuxin Liu², Ru-Sen Lu^{3,4,5}, Yosuke Mizuno^{6,7}, Jing Shu^{1,8,9,10,11,12}, Xiao Xue^{1,8}, Qiang Yuan^{13,14,10}, Yue Zhao¹⁵

¹CAS Key Laboratory of Theoretical Physics, Institute of Theoretical Physics, Chinese Academy of Sciences, Beijing 100190, China

²Department of Physics, Tsinghua University, Beijing 100084, China

³Shanghai Astronomical Observatory, Chinese Academy of Sciences, Shanghai 200030, China

⁴Key Laboratory of Radio Astronomy, Chinese Academy of Sciences, Nanjing 210008, China

⁵Max-Planck-Institut für Radioastronomie, Auf dem Hügel 69, D-53121 Bonn, Germany

⁶Tsung-Dao Lee Institute and School of Physics and Astronomy, Shanghai Jiao Tong University, Shanghai, 200240, China

⁷Institute for Theoretical Physics, Goethe University Frankfurt, Frankfurt am Main, 60438, Germany

⁸School of Physical Sciences, University of Chinese Academy of Sciences, Beijing 100049, China

⁹CAS Center for Excellence in Particle Physics, Beijing 100049, China

¹⁰Center for High Energy Physics, Peking University, Beijing 100871, China

¹¹School of Fundamental Physics and Mathematical Sciences, Hangzhou Institute for Advanced Study, University of Chinese Academy of Sciences, Hangzhou 310024, China

¹²International Center for Theoretical Physics Asia-Pacific, Beijing/Hangzhou, China

¹³Key Laboratory of Dark Matter and Space Astronomy, Purple Mountain Observatory, Chinese Academy of Sciences, Nanjing 210023, China

¹⁴School of Astronomy and Space Science, University of Science and Technology of China, Hefei 230026, China

¹⁵Department of Physics and Astronomy, University of Utah, Salt Lake City, UT 84112, USA

The hitherto unprecedented angular resolution of the Event Horizon Telescope (EHT) has created exciting opportunities in the search for new physics. Recently, the linear polarization of radiation emitted near the supermassive black hole M87* was measured on four separate days, precisely enabling tests of the existence of a dense axion cloud produced by a spinning black hole. The presence of an axion cloud leads to a frequency-independent oscillation in the electric vector position angle (EVPA) of this linear polarization. For a nearly face-on M87*, this oscillation in the EVPA appears as a propagating wave along the photon ring. In this paper, we leverage the azimuthal distribution of EVPA measured by the EHT to study the axion-photon coupling. We propose a novel differential analysis procedure to reduce the astrophysical background, and derive stringent constraints on the existence of axions in the previously unexplored mass window $\sim (10^{-21} - 10^{-20})$ eV.

1 Introduction

Via the technique of very long baseline interferometry, the Event Horizon Telescope (EHT) reaches an unprecedented spatial resolution in the radio-frequency band, imaging the horizon-scale structure of the supermassive black hole (SMBH) M87*¹⁻⁴. Such an achievement provides unique oppor-

tunities to study physics in extreme conditions. In particular, the EHT measures electromagnetic radiation at a wavelength of 1.3 millimeter, which is optimal for studying the magnetic field around such black holes via polarization measurements. Such measurements have been performed very recently⁵, revealing the magnetic field structure near the event horizon⁶.

Beyond the astrophysics in the vicinity of an SMBH, such as the accretion flow and jet, polarization measurements can also help us probe new physics beyond the Standard Model of particle physics. The axion is one of the best-motivated candidates for physics beyond the Standard Model, arising initially as a solution to the strong CP (charge-conjugation and parity) problem⁷⁻¹⁰. Axion-like particles are furthermore generically predicted in fundamental theories with extra dimensions¹¹, and are excellent dark matter candidates¹²⁻¹⁴. In Ref. ¹⁵, the authors proposed that the temporal and spatial variations of the electric vector position angle (EVPA) around the photon ring of an SMBH can be used to study the existence of an axion cloud produced by the superradiance mechanism¹⁶⁻¹⁸, thanks to the axion-induced birefringence effect^{19,20}. The search is sensitive to axion clouds with non-negligible self-interaction²¹⁻²⁴, which is complimentary to constraints from black hole spin measurements²⁵.

More explicitly, the EHT collaboration presented fiducial polarimetric images for four days (April 5/6/10/11 2017) in Ref. ⁵, along with the azimuthal distribution of the EVPA, including systematic uncertainties, for two days (April 5/11, 2017). Based on the search strategy proposed in Ref. ¹⁵ and the information provided in Ref. ⁵, we adopt an improved search strategy using differential EVPA in the time domain. Such a method can effectively reduce the uncertainties from the astrophysical background. In addition, we include more realistic modelling of the accretion flow and radiative transfer calculation of polarized light.

We demonstrate that the newly released EHT polarimetric measurements provide a powerful probe for studying the axion-photon coupling for axions masses near 10^{-20} eV. Interesting constraints, surpassing those from other measurements, can already be produced with the published EHT results. The sensitivity can be also significantly improved when more detailed information becomes available.

2 Axion Cloud-Induced Birefringence Effect

If the Compton wavelength of an ultralight boson, e.g., the axion in this study, is comparable to the gravitational radius of a rapidly spinning Kerr black hole, a bound state between the axions and the black hole can be spontaneously generated by extracting the black hole's rotational energy¹⁶⁻¹⁸. The growth of such a bound state is exponential. This is the so-called superradiance mechanism. Such a bound state is a close analog to a hydrogen atom, with discrete energy levels and a 'fine structure constant' $\alpha \equiv r_g/\lambda_c$, where r_g is the gravitational radius of the black hole and λ_c is the reduced Compton wavelength of the axion. The nontrivial self-interaction of the axion can halt the exponential growth, and the peak value of the axion field may become comparable to the decay constant f_a ²¹⁻²⁴. In such a scenario, the axion cloud around the black hole may lead to a region with the highest possible axion density anywhere in the universe.

Analogously to the hydrogen atom, the axion cloud can populate states with differing angular momentum quantum numbers, (l, m) . The mode with $(l, m) = (1, 1)$ is the lowest energy state amongst those satisfying the superradiant condition. Out of all possible states populated through superradiance, it has a peak located closest to the horizon of the BH. For an extreme Kerr black hole, α needs to be smaller than 0.5 in order for the $(1, 1)$ state to be populated. In this study we focus on the SMBH M87*, and consider the axion mass window from 2×10^{-21} eV to 10^{-20} eV, which gives α from 0.1 to 0.5. These axions in the cloud are non-relativistic, oscillating coherently with a frequency approximately equal to the axion mass m_a . A tighter upper bound on α depends on the spin of the black hole, as we will discuss later and in **Methods**. The lower bound on α is set by requiring the superradiant timescale to be much smaller than the age of the universe²⁶, i.e., within the range of 10^9 years in this study. It corresponds to an oscillation period of the axion cloud wavefunction shorter than 20 days. We note that the axions in the mass window studied here are unlikely to be the QCD axion, but rather axion-like particles.

Due to the axion-photon coupling $g_{a\gamma} a F_{\mu\nu} \tilde{F}^{\mu\nu} / 2$ where $F_{\mu\nu}$ is the field strength tensor of the photon and $\tilde{F}^{\mu\nu}$ is the dual tensor, the temporal and spatial variations of an axion background field induce a change in the dispersion relation of photons. Thus the EVPA of a linearly polarized photon, labeled as χ , experiences a rotation due to the axion background as

$$\Delta\chi = g_{a\gamma} [a(t_{\text{obs}}, \mathbf{x}_{\text{obs}}) - a(t_{\text{emit}}, \mathbf{x}_{\text{emit}})], \quad (1)$$

depending only on the axion field values at the emission and observation points^{19,20}. A generalization to curved spacetime was discussed in Ref.²⁷, reaching the same conclusion. We emphasize that this simple expression only holds for photons propagating in vacuum, when the photon wavelength is much smaller than the axion's Compton wavelength. In-medium effects need to be included by solving the radiative transfer equations along the photon path in more realistic cases.

The axion density around the Earth is negligible compared with that of an axion cloud surrounding M87*, and hence can be neglected. Without including in-medium effects, for a linearly polarized photon emitted at (t, r, θ, ϕ) in the Boyer-Lindquist (BL) coordinates of the black hole, its EVPA shift is directly related to the wavefunction of the axion cloud¹⁵

$$\Delta\chi(t, r, \theta, \phi) \approx -\frac{bcR_{11}(r) \sin\theta \cos[\omega t - \phi]}{2\pi R_{11}(r_{\text{max}})}. \quad (2)$$

For a fixed SMBH, the radial wave-function $R_{11}(r)/R_{11}(r_{\text{max}})$ depends on the axion mass. $b \equiv a_{\text{max}}/f_a$ is introduced to describe the peak value of the axion cloud; due to nontrivial self-interaction, both numerical simulations²¹⁻²³ and analytic estimates²⁴ indicate that $b \sim O(1)$ in the parameter space we are interested in. The parameter c relates the axion-photon coupling $g_{a\gamma}$ to the decay constant f_a via $c \equiv 2\pi g_{a\gamma} f_a$, and it is the fundamental quantity that this work constrains.

In reality, plasma effects also need to be accounted for to properly model the variation of the EVPA. In particular, the axion-induced birefringent effect should be combined with astrophysical Faraday rotation. As a consequence, the Faraday rotation coefficient obtains an additional contribution, i.e., $\rho_V = \rho_V^{\text{FR}} - 2g_{a\gamma} \frac{da}{ds}$ where s is the proper time. The first term ρ_V^{FR} describes the

frequency-dependent Faraday rotation induced by the plasma effect. The second term is from the axion field, which is an additional frequency-independent contribution along the line-of-sight. The summation of these two effects characterizes the phase variation in $Q + iU$, where Q and U are the Stokes parameters for the linear polarization.

In this study, we model the accretion disk by the analytic radiatively inefficient accretion flow (RIAF)²⁸ with a sub-Keplerian velocity distribution and vertical magnetic field⁶. The thickness of the accretion flow is parametrized by a dimensionless quantity $H \equiv h/R$. Here h is the height scale, and R is the horizontal scale of the accretion flow. We take H as 0.3 and 0.05 for a magnetically arrested disk (MAD)^{29–32}. The normalization of the electron density is set to be $\sim 10^5 \text{ cm}^{-3}$ so that the total flux density at 230 GHz is about 0.5 Jy^{1-4} and the magnetic field strength is consistent with EHT estimates⁶.

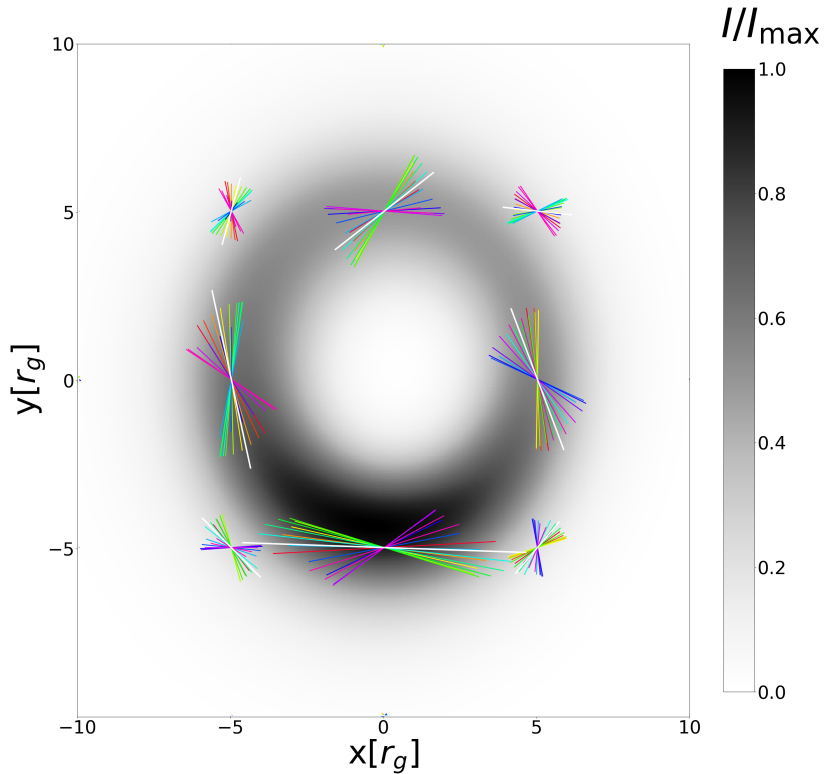


Figure 1: **Illustration of the IPOLE simulation of polarized emission from a Kerr black hole surrounded by an axion cloud.** For axion parameters we take $\alpha = 0.4$, and $g_{a\gamma}a_{\text{max}} = 3\pi/4$ as a benchmark. An analytic RIAF with $H = 0.3$, vertical magnetic field, and sub-Keplerian velocity distribution are assumed. The white quivers are the EVPAs without the axion-induced birefringence effect at each point. Different colors, ranging from red to purple, represent the EVPA time variation when the axion cloud exists. The $+x$ axis is taken to be aligned with the direction of jet projection on this plane.

As an illustration, we consider the SMBH M87* at a 17° inclination angle with respect to the

sky plane. The quivers in Fig. 1 show the EVPA variations using the polarized radiation transfer code `IPOLE`^{33,34}. The length of each quiver is proportional to the intensity of the linear polarization, i.e., $\sqrt{Q^2 + U^2}$, and the direction indicates the polarization direction. The white quivers show the values of EVPA without the axion-induced birefringence effect. One oscillation period of the axion cloud is equally divided into 16 segments, and the color of each quiver, from red to purple, represents the time evolution.

3 Variations of the Azimuthal EVPA Pattern

On the sky plane, we use the polar coordinates (ρ, φ) with the origin at the black hole center. The axis with $\varphi = 0$ is taken to be aligned with the direction of jet projection on this plane. In order to compare with the data, we follow Ref.⁵ and calculate the intensity weighted average EVPA as a function of φ on the sky plane,

$$\langle \chi(\varphi) \rangle \equiv \frac{1}{2} \arg \left(\langle Q \times I \rangle + i \langle U \times I \rangle \right). \quad (3)$$

The intensity weighted average region is taken to be between $\rho_{\text{in}} \simeq 3r_g$ and $\rho_{\text{out}} \simeq 8r_g$, according to Ref.².

The axion-induced birefringence effect leads to an oscillation in $\langle \chi(\varphi) \rangle$. For the $l = m = 1$ state, this variation can generically be parametrized as

$$\Delta \langle \chi(\varphi) \rangle = -\mathcal{A}(\varphi) \cos [\omega t + \varphi + \delta(\varphi)]. \quad (4)$$

In Fig. 2, we show results from the `IPOLE` calculations with $H = 0.05$ and $H = 0.3$ as two representative models. We study the φ -dependence of the relative phase δ as well as the amplitude \mathcal{A} which is normalized to $g_{a\gamma} a_{\text{max}} \equiv bc/2\pi$.

We note that $\delta(\varphi)$ is well approximated by a cosinusoidal function, specifically

$$\delta(\varphi) \approx -\omega r_{\text{ring}} \sin 17^\circ \cos \varphi + \delta_0. \quad (5)$$

where δ_0 is the arbitrary initial phase of the axion cloud. r_{ring} is approximately the radius of the ring, i.e., $\sim 5 r_g$, where the dominant emission comes from. This indicates that $\delta(\varphi)$ arises from the emission time delay due to the 17° inclination angle between the M87* spin direction and the sky plane. In addition, such a fit is also a reliable verification of the mapping between φ on the sky plane and ϕ in BL coordinates, as discussed in **Methods**.

The behaviour of $\mathcal{A}(\varphi)$ is more subtle, owing to several aspects which must necessarily be considered. Firstly, there is an important washout effect along the line of sight. The accretion flow is optically thin in our study, and thus photons that reach the Earth simultaneously were emitted at different times along the line of sight. Since the axion field oscillates at a frequency $\omega \simeq m_a$, these photons experience different axion cloud phases at their time of emission, resulting in a washout effect for $\mathcal{A}(\varphi)$, especially when the radiation size S_r is larger than the Compton

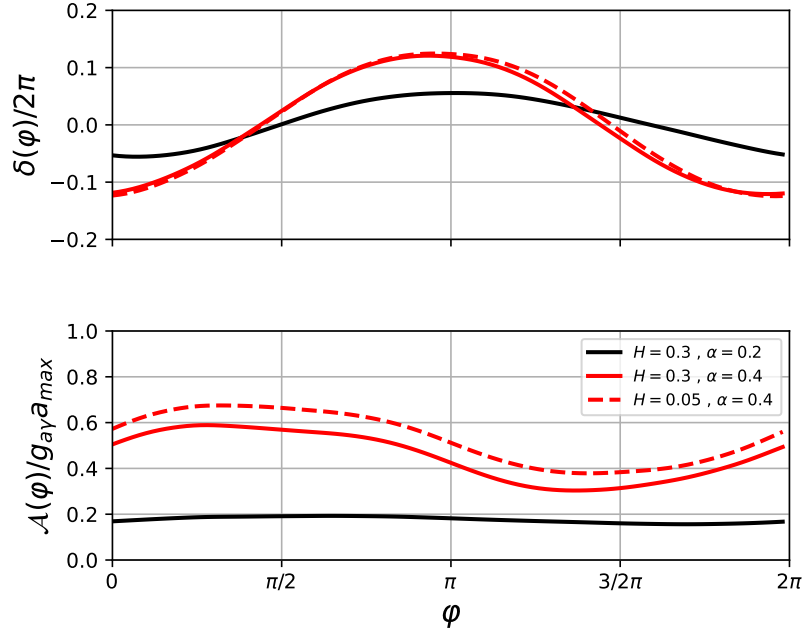


Figure 2: **The relative phase $\delta(\varphi)/2\pi$ and amplitude $\mathcal{A}(\varphi)/g_{a\gamma}a_{\max}$ of the $\langle\chi(\varphi)\rangle$ variation.** The black hole spin is assumed to be 0.99, and the accretion flow is modelled as analytic RIAF using IPOLE, with vertical magnetic field and sub-Keplerian velocity distribution. Different choices of H and α are shown in the plot. $\varphi = 0$ corresponds to the position angle of the jet projection.

wavelength $2\pi\lambda_c$ (see **Methods** for a more detailed description and Figure 4 for an illustration of a case where emissions and the amplitude of the axion field are constant within a region with size S_r). A decrease of H from 0.3 to 0.05 reduces this effect slightly, and so we choose $H = 0.3$ as a conservative benchmark for the rest of the discussion.

The other important washout effect comes from the lensed photons that experience a much longer propagation time than those directly emitted from the accretion flow. The axion-induced EVPA variations for these photons do not add up coherently. For a smaller value of α the Compton wavelength is longer, and the washout effect hence less severe. However, $\mathcal{A}(\varphi)/g_{a\gamma}a_{\max}$ becomes smaller with a smaller α (see the black line in Fig. 2). This is mainly because the emission ring is more spatially separated from the axion cloud peak, and the suppression factor $R_{11}(r)/R_{11}(r_{\max})$ becomes smaller.

Finally, the smearing due to the finite angular resolution of the EHT observation also leads to a washout effect along the φ -direction¹⁵.

4 Differential EVPA and Axion Constraints

The EHT collaboration has released the fiducial polarimetric images from four days, i.e., April 5, 6, 10 and 11, 2017⁵. For each of the days, there are maps presenting the EVPA distribution as well as the linear polarization intensity. In addition, for two of the four days, April 5 and 11, the intensity weighted EVPA, $\langle\chi(\varphi)\rangle$, as functions of the azimuthal angle are also provided. Along the φ -axis, $\langle\chi(\varphi)\rangle$ is obtained by taking the average of a wedge with an opening angle of 10° .

As discussed previously, we are looking for an overall pattern of EVPA variation across the azimuthal angle of the polarized emission. It is natural to expect that the astrophysical backgrounds of two sequential days do not change remarkably⁵. Thus we group the 4-day observations into two pairs, (April 5, 6) and (April 10, 11). For each pair, we study the variation of $\langle\chi(\varphi)\rangle$ along the azimuthal direction, i.e., $\langle\chi(\varphi, t_j)\rangle - \langle\chi(\varphi, t_i)\rangle$ where t_i and t_j represent the two sequential days with interval $t_{\text{int}} \equiv t_j - t_i = 1$ day. To investigate whether there is an evidence of axion-induced birefringent effect we compare the $\langle\chi(\varphi, t_j)\rangle - \langle\chi(\varphi, t_i)\rangle$ obtained in each pair of days with the theoretical prediction due to the axion field.

In the fiducial linear polarization images, there are slight differences between the two sequential days. It is not clear whether such differences are induced by the intrinsic variation of the accretion flow or by the change of the baseline coverage⁵. Thus in our analysis, we treat the central value of $\langle\chi(\varphi, t_j)\rangle - \langle\chi(\varphi, t_i)\rangle$ as zero. Furthermore, we assume that the reconstruction uncertainties for the two sequential days remain the same but uncorrelated. Thus the error bar of $\langle\chi(\varphi, t_j)\rangle - \langle\chi(\varphi, t_i)\rangle$ is simply that of $\langle\chi(\varphi, t_i)\rangle$ multiplied by a factor of $\sqrt{2}$.

Meanwhile, $\langle\chi(\varphi, t_j)\rangle - \langle\chi(\varphi, t_i)\rangle$ for the two pairs of sequential days are related. Firstly, $\mathcal{A}(\varphi)$ characterizes the difference in the EVPA variation amplitude for two sequential days, and to a good approximation $\mathcal{A}(\varphi)$ for the two pairs is the same. Furthermore, the phases of the axion field at the times of two pairs are related to each other by a relative phase difference of $(\omega \times 5 \text{ days})$. This correlation is accounted for in our analysis.

For each value of m_a , we calculate the likelihood values for different $g_{a\gamma}a_{\text{max}} \equiv bc/2\pi$. Throughout the analysis, the axion field phase δ_0 is treated as a nuisance parameter and is marginalized over $[0, 2\pi]$. The black hole spin is assumed to be either 0.99 or 0.80³⁵⁻³⁷. This determines the upper limit of α that we can probe in this study to be 0.44 or 0.25 respectively. The lower limit of α is taken to be 0.1. With a smaller α , the peak of the axion cloud is too far away from the photon ring, and the superradiance timescale becomes longer than the age of the universe. In Fig. 3, we present the 95% credible level upper limit on the axion-photon coupling, characterized by the value of c . Here we assume that the axion cloud has saturated, i.e., $b = 1$. The bound becomes weaker for smaller axion masses. This is due to a smaller value of the suppression factor $R_{11}(r)/R_{11}(r_{\text{max}})$, as well as a smaller 1-day axion field variation due to the longer oscillation period.

We also compare our constraints with the bounds from CAST³⁸, Supernova 1987A³⁹, super star clusters⁴⁰, the M87 Galaxy⁴¹, and NGC1275⁴². While all these existing studies put constraints on $g_{a\gamma}$, our result provides a novel probe to the conversion factor, i.e., $c \equiv 2\pi g_{a\gamma} f_a$. This is because

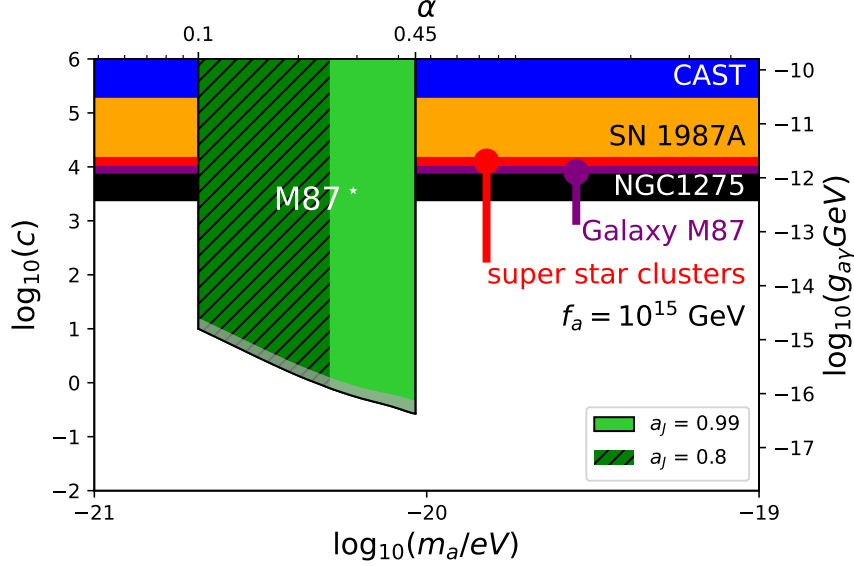


Figure 3: **The 95% credible level upper limit (green) on the axion-photon coupling, characterized by $c \equiv 2\pi g_{a\gamma} f_a$, derived from the EHT polarimetric observations of SMBH M87***. The black hole spin a_J is assumed to be 0.99 or 0.80. The latter case corresponds to a smaller mass window, which overlaps with $a_J = 0.99$ case in the lower mass region. The gray band at the bottom represents the uncertainty from the five different EVPA reconstruction methods. The bounds from CAST³⁸, Supernova 1987A³⁹, super star clusters⁴⁰, the M87 Galaxy⁴¹, and NGC1275⁴², assuming $f_a = 10^{15}$ GeV, are shown for comparison.

the axion field saturates the largest possible value in the axion cloud, thereby providing a useful complementarity to the existing landscape of axion searches. In terms of the axion models, the value of c is related to the anomaly coefficients in the ultraviolet theory. In addition, an exponentially large value of c can appear in models of the clockwork axion^{43,44}. In order to directly compare our results with others, we take f_a to be 10^{15} GeV as a benchmark, motivated by theories of Grand Unification. For the axion mass window we consider, a large region of previously unexplored parameter space is covered by the EHT observations. The previous constraints are improved upon by several orders of magnitude, as shown in Fig. 3. We note that our constraints are stronger yet for larger values of f_a . However, they are not necessarily applicable beyond f_a at 10^{16} GeV since the axion self-interaction becomes too weak to prevent superradiance²⁵, and the axion field value does not necessarily saturate.

5 Conclusions and Future Prospects

Polarized imaging of the vicinity of SMBHs offers a unique probe to search for axions, thanks to the EVPA oscillation of linearly polarized photons arising from the axion-induced birefringence effect. In this study we introduced a novel data analysis method that may significantly reduce the astrophysical background, and applied it to four days of polarization measurements of M87* by the EHT⁵. EHT observations can as a result rule out a region of the axion mass and axion-photon coupling parameter space, which is unexplored by previous experiments.

We emphasize that a further optimized search strategy could be applied with improved measurements and analysis of the emitted polarization, e.g., the upcoming EHT observations with higher time cadence or the Next Generation EHT (ngEHT) in the future. Firstly, increasing the overall statistics would definitely improve the sensitivity, by incorporating more available pairs of sequential days for our differential analysis and EVPA reconstruction with higher precision. Further gains can also be made if the results were provided in shorter time segments within one day. Furthermore, since the axion-induced birefringence effect is independent of the photon frequency, polarization measurements at different frequency bands such as 345 GHz will be extremely helpful to distinguish the axion-induced effect from Faraday rotation in the plasma. The radial distributions of the EVPA are also valuable, and the sensitivity could be improved by using a fuller modelling of the axion profile. Finally, we note that the EVPA observed outside the photon ring is free from the contamination of lensed photons, which give the dominant contribution to the washout effect. Removing these lensed photons would help to provide a universal signal prediction, independent of accretion flow models. All these improvements are within expectations of either the future EHT data release or the ngEHT with an increased baseline coverage⁴⁵.

Methods

Black Hole Superradiance Through the superradiance mechanism, a rapidly spinning black hole can generate an exponentially growing axion cloud, if the axion has a reduced Compton wavelength λ_c comparable to the gravitational radius of the Kerr black hole r_g ^{16–18,26,46–49} (for a review see Ref.⁵⁰). Such a process is terminated by either the axion self-interaction or a sufficient loss of the angular momentum of the black hole. The wave-function of the axion cloud can be written as

$$a(x^\mu) = e^{-i\omega t} e^{im\phi} S_{lm}(\theta) R_{lm}(r), \quad (6)$$

where $x^\mu = [t, r, \theta, \phi]$ are the Boyer-Lindquist (BL) coordinates. Such a bound state formed by the black hole and the axion cloud is closely analogous to a hydrogen atom, with the coupling constant being $\alpha \equiv r_g/\lambda_c$. The θ dependence is characterized by the spheroidal harmonics S_{lm} which simplify to Y_{lm} in the non-rotating limit of the black hole, or the non-relativistic limit of the axion cloud. $R_{lm}(r)$ is the radial component of the wave function that vanishes at both the horizon of the black hole and at infinity. For a benchmark axion with Compton wavelength satisfying $\alpha = 0.4$, the cloud peaks close to the region where the dominant emissions come from¹⁵. Since the radius at which the axion field reaches the maximum, r_{\max} , scales as $1/\alpha^2$, r_{\max} becomes larger for smaller values of α .

The highest superradiant rate happens for $l = 1, m = 1$, which is the lowest energy state amongst those satisfying the superradiance condition²⁶. In this case, for all values of θ , the axion cloud wavefunction peaks at the equatorial plane of the black hole, i.e., $\sin \theta = 1$. r_{\max} becomes larger for higher modes with a bigger azimuthal number l . To be conservative, we only focus on the $(1, 1)$ state and do not consider higher modes in this study.

The range of the superradiance condition for α is sensitive to the black hole spin a_J , which is still uncertain for M87*⁵. Refs.^{35,36} claim M87* to be a nearly extremal Kerr black hole. From

a recent synthetic modeling study of M87 jet at 86 GHz, higher black hole spin is favored.⁵¹ Thus in this study, we take the black hole spin a_J to be 0.99 and 0.8³⁷ as two benchmarks. For a fixed azimuthal mode m and black hole spin a_J , the superradiance condition imposes an upper limit on α ²⁶,

$$\alpha < \frac{a_J m}{2 \left(1 + \sqrt{1 - a_J^2}\right)}, \quad (7)$$

With $m = 1$, α can be at most 0.5 for an extremal Kerr black hole and 0.25 if $a_J = 0.8$. We set a lower limit on α of 0.1, so that the superradiant timescale is much shorter than the age of the universe, i.e., within the range of 10^9 years. The black hole spin can be as low as $a_J = 0.5$ ²⁶ in order to satisfy the superradiance condition for $\alpha = 0.1$. Once this is met the axion cloud profile is only slightly influenced by the value of a_J , with α being fixed⁵².

The robustness of the axion cloud is discussed in Ref.¹¹, where several potential effects which may destroy the axion cloud are discussed. The tidal forces from a companion star turn out to be negligible. The metric is always dominated by the SMBH, especially for our region of interest. One may also be concerned about the possibility of a merger with another SMBH in the past, however, we mainly focus on the axion mass range with relatively short timescales for superradiance. Even if such a drastic merger happened once the axion cloud should have enough time to build up again, and thus we neglect this possibility in our study.

With the growth of the axion cloud, the axion field value gets close to the decay constant f_a that governs the self-interaction of axions from the axion potential $V(a) = m_a^2 f_a^2 (1 - \cos a/f_a)$, where m_a is the mass of the axion. Due to nontrivial self-interactions, the superradiance is terminated. Consequently the axion cloud enters a self-interaction dominated regime, and black hole spin measurements would not apply anymore^{25,37,53-56}. The fate of the axion cloud can either be a violent bosonova or a saturated phase^{21-24,57}. Interestingly, in either case, the numerical simulations²¹⁻²³ and the analytic estimates²⁴ show that the maximum of the field value a_{\max} remains close to f_a as long as the saturation regime is reached. This leaves our conclusion insensitive to this subtlety. We introduce $b \equiv a_{\max}/f_a$ to describe the peak value of the axion cloud. We note that in Ref.²⁴, the value of b is shown to decrease at lower α and logarithmically dependent on the mass of the black hole.

Accretion Flow and Radiative Transfer For low-luminosity active galactic nuclei, such as Sgr A* and M87*, the accretion flow are approximately described as radiatively inefficient accretion flow (RIAF)^{58,59}, which are geometrically thick and optically thin at 230 GHz^{4,59,60}. The accretion flow thickness is characterized by a dimensionless quantity $H \equiv h/R$ where h is the height scale and R is the horizontal scale of the accretion flow²⁸. For a magnetically arrested disk (MAD), which well-describes M87*⁶, H is compressed to be 0.05 by the strong magnetic field in the inner region ($\lesssim 10 r_g$) and becomes ~ 0.3 in the outer region²⁹⁻³². In this study we adopt the analytic RIAF model²⁸ as a benchmark model, and vary H in order to understand the uncertainties induced by the thickness of the accretion flow. As demonstrated later, a different choice of H does not change our conclusion qualitatively.

The Stokes parameters (I, Q, U, V) are generically applied to describe the properties of macroscopic polarization (see e.g., Ref. ⁶¹), in which I is the total intensity, Q and U characterize the linear polarization, and V describes the circular polarization. The in-medium effects lead to mixtures among the four Stokes components in the polarized radiative transfer equation

$$\frac{d}{ds} \begin{pmatrix} I \\ Q \\ U \\ V \end{pmatrix} = \begin{pmatrix} j_I \\ j_Q \\ j_U \\ j_V \end{pmatrix} - \begin{pmatrix} \alpha_I & \alpha_Q & \alpha_U & \alpha_V \\ \alpha_Q & \alpha_I & \rho_V & \rho_U \\ \alpha_U & -\rho_V & \alpha_I & \rho_Q \\ \alpha_V & -\rho_U & -\rho_Q & \alpha_I \end{pmatrix} \begin{pmatrix} I \\ Q \\ U \\ V \end{pmatrix}, \quad (8)$$

where s is the proper time, $j_{I,Q,U,V}$ are the polarized emissivities, $\alpha_{I,Q,U,V}$ are the absorption coefficients, and $\rho_{Q,U,V}$ are the Faraday rotation and conversion coefficients.

The axion-induced birefringence effect can be properly included in the radiative transfer matrix as

$$\rho_V = \rho_V^{\text{FR}} - 2g_{a\gamma} \frac{da}{ds}, \quad (9)$$

where the first term is the coefficient of the frequency-dependent Faraday rotation from the plasma, and the second term is from the axion field which gives a frequency-independent addition along the line-of-sight. ρ_V characterizes the rotation of the phase in $Q + iU$ ^{19,20,62-68}, which is related to the EVPA through

$$\chi \equiv \frac{1}{2} \arg(Q + iU). \quad (10)$$

To properly model the axion-induced birefringence effect, we modify the polarized radiative transfer equation in the general relativistic radiation transfer code `IPOLE`^{33,34}, as indicated in Eq. (9), with analytic RIAF models in which $H = 0.05$ and 0.3 are implemented. For the velocity distribution, we choose the sub-Keplerian flow as an approximation. The magnetic field is taken to be vertical as a benchmark model⁶. In addition, we adjust the normalization of the electron density to be $\sim 10^5 \text{ cm}^{-3}$ compared to the original model so that the total flux density in the image at 230 GHz is about 0.5 Jy^{1-4} and the magnetic field strength is consistent with the EHT estimate⁶. We also perform a more comprehensive study in order to investigate the effects of various choices in the RIAF model, such as the direction of the magnetic field (e.g., toroidal or radial) and the velocity distributions. We find that varying these parameters does not affect our conclusion qualitatively.

The accretion flow, on the other hand, may also be affected by the black hole spin. Taking sub-Keplerian RIAF as the benchmark model, we compare the axion cloud induced EVPA time variations with different choices of the black hole spin, $a_J = 0.5$ and $a_J = 0.8$. We set the value of α to be close to 0.1 in order to satisfy the superradiance condition Eq. (7). We find that the EVPA variations remain qualitatively the same as those in the scenario with $a_J = 0.99$. This is due to the fact that the line-of-sight washout effect becomes negligible for a lower value of α , i.e., longer Compton wavelength. More details will be discussed later in the **Line-of-Sight Washout Effect** Section in **Methods**.

In order to compare with EHT data, we need to map the sky plane coordinates (ρ, φ) to the BL coordinates of the SMBH. This can be done through ray-tracing in `IPOLE`. For an MAD, the

dominant emission comes from the region near the equatorial plane of the black hole. Combined with the fact that the brightest region is around $5 r_g$ away from the center of the black hole, for SMBH M87* whose orientation is almost face-on, φ can be directly mapped to $-\phi$ in BL coordinates to a good approximation. The minus sign is due to the fact that the spin direction of M87* points away from the Earth, i.e., M87* rotates clockwise on the sky plane. In addition, for the region of interest in this study ρ can be approximately mapped to r in BL coordinates as well; $\rho \simeq r$.

There are also photons that propagate around the black hole several times before reaching the Earth due to lensing effects⁶⁹⁻⁷², which can influence the polarization as well⁷³. For the total intensity they contribute subdominantly, providing $\sim 10\%$ at most. However, if one uses the intensity weighted EVPA as the observable, their contribution is non-negligible and can lead to a noticeable washout of the axion-induced birefringence, which contributes to the asymmetry along φ in Fig. 2. We note that such a washout effect can be largely removed if the detailed EVPA distribution is provided at different ρ .

Data Characterization To calculate $\langle \chi(\varphi, t_j) \rangle - \langle \chi(\varphi, t_i) \rangle$, one has to take into account the observation time in each day, i.e., $t_{\text{obs}} \simeq 6$ hours. Using the parametrization in Eq. (4), we have

$$\begin{aligned}
& \langle \chi(\varphi, t_j) \rangle - \langle \chi(\varphi, t_i) \rangle \\
&= \frac{\mathcal{A}(\varphi)}{t_{\text{obs}}} \int_{-t_{\text{obs}}/2}^{t_{\text{obs}}/2} \{ \cos [\omega(t_i + \delta t) + \varphi + \delta(\varphi)] \\
&\quad - \cos [\omega(t_j + \delta t) + \varphi + \delta(\varphi)] \} d\delta t \\
&= \widetilde{\mathcal{A}}(\varphi) \sin [\omega(t_i + t_{\text{int}}/2) + \varphi + \delta(\varphi)]
\end{aligned} \tag{11}$$

where $\widetilde{\mathcal{A}}(\varphi) = 2\mathcal{A}(\varphi) \sin [\omega t_{\text{int}}/2] \sin [\omega t_{\text{obs}}/2] / (\omega t_{\text{obs}}/2)$. The factor $\sin [\omega t_{\text{obs}}/2] / (\omega t_{\text{obs}}/2)$ represents the washout effect due to the time averaging over the observation time of each day, while $\sin [\omega t_{\text{int}}/2]$ represents how much the axion cloud has changed during the time interval of a given day. For the parameter space we are interested in, the axion oscillation period is larger than one day. Thus $\sin [\omega t_{\text{int}}/2]$ contributes as a suppression factor, which makes the constraints in the lower mass region weaker in Fig. 3. Finally, we note that one can absorb $\omega(t_i + t_{\text{int}}/2)$ into the phase of the axion cloud δ_0 , which is a nuisance parameter in the analysis.

In Fig. 8 of Ref. ⁵, $\langle \chi(\varphi) \rangle$ is constructed using five different methods. The obtained results do not perfectly agree with each other, reflecting possible differences in the systematic uncertainties of each analysis. However, we are mainly interested in the time variation of the EVPA. We therefore assume that these systematics can be largely eliminated for this differential study.

The reconstruction of $\langle \chi(\varphi) \rangle$ from the data is subtle. For example, there are nontrivial leakages between the polarization modes in the measurements, characterized by the so-called D-term. These can lead to uncertainties in $\langle \chi(\varphi) \rangle$. For some values of φ (particularly when the polarized intensity is low), the reconstruction gives ambiguous results, which appear as bifurcations in the figure. In our analysis we apply a conservative approach, removing the range of φ where reconstruction ambiguities appear. We choose a bin-size of 10° in order to reduce the correlations among

different azimuthal angles. We only keep the bins whose EVPA distribution can be properly fit by a Gaussian function without ambiguous bifurcations. For example, in the results produced by the `polsolve` method⁷⁴, the left bins have azimuthal angles ranging between 30° to 90° and 170° to 330° for the April 5 data, and 30° to 310° for the April 11 data. Effectively we then have 53 bins in total. For each bin, we fit the stripe width by a Gaussian function to obtain an estimation of the measurement error. The errors roughly range from $\pm 3^\circ$ to $\pm 15^\circ$. For other methods the uncertainties in the regions with strong intensity are nearly the same, and thus they give comparable axion constraints as those shown in Fig. 3.

Statistics We use Bayesian statistics to derive the 95% credible level (C.L.) upper limits on the axion-photon coupling, characterized by c , for different axion masses m_a (or equivalently, α , for a given black hole mass). The marginalized posterior of c is written as

$$\Pr(\log_{10} c | \mathbf{d}, m_a) = \frac{1}{\text{Const}} \int_0^{2\pi} \frac{d\delta_0}{2\pi} \prod_i \frac{1}{\sqrt{2\pi}\sigma_i} e^{-(d_i - d_i^0(c, m_a, \delta_0))^2 / (2\sigma_i^2)}, \quad (12)$$

where we assume that the priors of the initial phase δ_0 and $\log_{10} c$ are uniform. The denominator, Const , is the normalization factor which does not need to be calculated in our case. In the exponent d_i represents the EVPA variation in a sequential-day pair in the experimental data, while the sub-index i runs over both the azimuthal angle bins and the two pairs, i.e., $\langle \chi(\varphi, \text{day6}) \rangle - \langle \chi(\varphi, \text{day5}) \rangle$ and $\langle \chi(\varphi, \text{day11}) \rangle - \langle \chi(\varphi, \text{day10}) \rangle$. The parameter $d_i^0(c, m_a, \delta_0)$ is the theoretical prediction of the EVPA variation, derived from Eq. (11), while σ_i characterizes the uncertainty in the data. As stated in Ref.⁵, no significant EVPA variations are observed in any sequential-day pairs, which indicates $d_i = 0$. We then perform the integration on the marginalized posterior in order to obtain the cumulative probability of $\log_{10} c_{\text{ul}}$, where c_{ul} is the upper limit of c to achieve a corresponding probability value,

$$\Pr(\log_{10} c < \log_{10} c_{\text{ul}} | \mathbf{d} = 0, m_a) = \int_{\log_{10} c_{\text{min}}}^{\log_{10} c_{\text{ul}}} \Pr(\log_{10} c | \mathbf{d} = 0, m_a) d \log_{10} c. \quad (13)$$

Here we choose $c_{\text{min}} = \alpha_{\text{EM}} \simeq 1/137$, given by the scenario with one species of charged fermion contributing to this anomaly vertex. Here α_{EM} is the electromagnetic fine structure constant. A lower value of c_{min} is possible and it will lead to tighter constraints. The 95% C.L. upper limit for $\log_{10} c$, denoted as $\log_{10} c_{95\%}$, is calculated by inversely solving the following equation

$$95\% = \frac{\Pr(\log_{10} c < \log_{10} c_{95\%} | \mathbf{d} = 0, m_a)}{\Pr(\log_{10} c < \log_{10} c_{\text{max}} | \mathbf{d} = 0, m_a)} \quad (14)$$

where we choose c_{max} to be a large number, such as 10^3 . We note that our result is not sensitive to this choice, and the normalization factor Const is also automatically cancelled in this calculation.

Of course, there are uncertainties from the time-dependent astrophysical background. The time variation of the accretion flow is not well understood, and consequently it is not included in our simulation discussed above. This leads to the major subtlety when we compare results from simulations with observations. For M87* with mass 6.5×10^9 solar masses¹⁻⁴, the typical time

scale is 5 days for light propagating near the innermost stable circular orbit (ISCO). In addition, for gas in the accretion flow with a sub-Keplerian velocity distribution, the associated time scale is approximately one month at $r \simeq 5r_g$. Thus it is reasonable to expect that the astrophysical features at large scales, comparable to the size of the accretion flow, remain approximately unchanged over a time scale of one day. The differential EVPA for two sequential days, i.e., $\langle \chi(\varphi, t_j) \rangle - \langle \chi(\varphi, t_i) \rangle$, is an ideal observable with the astrophysical uncertainties being highly suppressed.

To qualitatively estimate this uncertainty among the azimuthal angle bins selected in our analysis, we find the common ones shared in April 5 and April 11 data, and calculate the differences between the average values of $\langle \chi(\varphi) \rangle$. Assuming the accretion flow dynamics lead to an approximately linear variation during the 6-day interval, we divide the difference in each bin by a factor of 6. This provides a rough estimate of the variation induced by the astrophysical background. By comparing it with the error bar derived for $\langle \chi(\varphi, t_j) \rangle - \langle \chi(\varphi, t_i) \rangle$, we find that the astrophysical background uncertainty is generally smaller than that from the EVPA reconstruction. This justifies the validity of our proposed analysis strategy.

Line of Sight Washout Effect Here we investigate in detail how the integral along the line of sight leads to a washout effect. As discussed previously, the axion-induced birefringence can be incorporated via a modification of the radiative transfer matrix. To gain some intuition, we simplify the problem by ignoring in-medium effects, keeping only the source terms and the axion effect. Then the evolution of the linear polarization can be written as

$$\frac{d(Q + iU)}{ds} = j_Q + i j_U - i2g_{a\gamma} \frac{da}{ds} (Q + iU). \quad (15)$$

This can be generally solved via

$$Q(s_f) + iU(s_f) = \int_{s_i}^{s_f} e^{i2g_{a\gamma}(a(s_f)-a(s))} (j_Q(s) + i j_U(s)) ds, \quad (16)$$

where s_i and s_f are the initial and final points along the line of sight. Further simplifying, we assume the radiation source terms, j_Q and j_U , are constant in a finite region. Thus the washout effect is characterized by the axion-dependent integral in Eq. (16). For a qualitative estimation, we take $a(s)$ to be a coherently oscillating background with a constant amplitude a_0 over the same region. The resulting washout effect on \mathcal{A} , defined in Eq. (4), is shown in Figure 4, as a function of the size of the radiation source S_r , normalized by the axion Compton wavelength $2\pi\lambda_c$. Here we see that the washout effect is negligible if $\lambda_c \gg S_r$, and it becomes sizable when these two scales are comparable.

In a realistic scenario like the optically thin accretion flow around M87*, S_r is determined by the geometric thickness of the accretion flow. The washout effect is not important if the accretion flow satisfies $r_{\text{ring}}H < 2\pi\lambda_c$. Taking $\alpha \equiv r_g/\lambda_c = 0.4$ and $r_{\text{ring}} \simeq 5r_g$, this condition becomes $H \ll 3$, which is easily satisfied in our RIAF model. For smaller α , due to the much larger λ_c , this washout effect along the line of sight is further reduced.

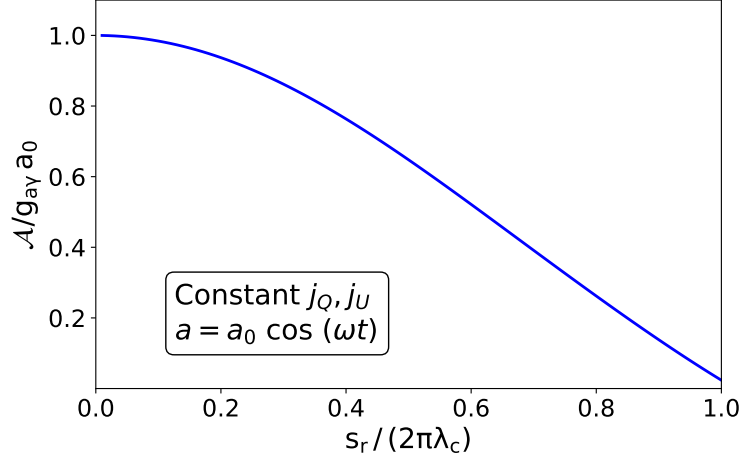


Figure 4: **Washout effect on the oscillation amplitude of the EVPA as a function of the size of the radiation source S_r , normalized by the axion Compton wavelength $2\pi\lambda_c$.** We assume the radiation source terms, j_Q and j_U , are constant in a finite region and take the axion field to be a coherently oscillating background with a constant amplitude a_0 over the region.

Furthermore, there are also contributions from lensed photons; since the dominant emission comes from around the equatorial plane, the observed photon ring contains radiation which has propagated around the black hole several times. Since the axion cloud had different phases when these photons were emitted, they also lead to washout effects to the EVPA variations, as shown in Fig. 2. We note that in more realistic cases, such as the accretion flow in the general relativistic magnetohydrodynamic simulations, the lensed photons are typically less polarized than the direct emission due to magnetic turbulence⁷³. Thus using the analytic RIAF as a benchmark in this study serves as a conservative estimation.

Acknowledgements We are grateful to Nick Houston, Samuel Liebersbach and Dimitrios Psaltis for careful reading and useful comments on the manuscript, and Chunlong Li, Ye-Fei Yuan, Shan-Shan Zhao and Zihan Zhou for useful discussions. Y.C. is supported by the China Postdoctoral Science Foundation under Grants No. 2020T130661, No. 2020M680688, the International Postdoctoral Exchange Fellowship Program, and by the National Natural Science Foundation of China (NSFC) under Grants No. 12047557. R.-S.L. is supported by the Max Planck Partner Group of the MPG and the Chinese Academy of Sciences (CAS), the NSFC under Grant No. 11933007, the Research Program of Fundamental and Frontier Sciences of CAS under Grant No. ZDBS-LY-SLH011, and the Shanghai Pilot Program for Basic Research ? Chinese Academy of Science, Shanghai Branch (JCYJ-SHFY-2021-013). Y.M. is supported by the ERC Synergy Grant “BlackHoleCam: Imaging the Event Horizon of Black Holes” under Grant No. 610058. J.S. is supported by the NSFC under Grants No. 12025507, No. 11690022, No. 11947302, by the Strategic Priority Research Program and Key Research Program of Frontier Science of CAS under Grants No. XDB21010200, No. XDB23010000, and No. ZDBS-LY-7003 and CAS project for Young Scientists in Basic Research YSBR-006. Q.Y. is supported by the NSFC under Grants No. 11722328, No. 11851305, by the Key Research Program of CAS under Grant No. XDPB15, and by the Program for Innovative Talents and Entrepreneur in Jiangsu. Y.Z. is supported by U.S. Department of Energy under Award No. DESC0009959. Y.C. would like to thank the SHAO and TDLI for their kind hospitality. Y.Z. would like to thank the ITP-

CAS for their kind hospitality.

Author Contributions JS, QY and YZ initiated this study, YC, XX and YZ developed the method, XX, YL and YC analyzed the data with important contribution from YM and RSL, YM offered guidance on accretion flow models, YC and YZ wrote the initial draft, with contributions from QY and JS. All authors have reviewed, discussed, and commented on the modeling, data analysis, and the manuscript. Correspondence and requests for materials should be addressed to YC (yifan.chen@itp.ac.cn), YM (mizuno@sjtu.edu.cn), JS (jshu@itp.ac.cn), QY (yuanq@pmo.ac.cn), and YZ (zhaoyue@physics.utah.edu).

Data Availability The data of polarimetric measurements used in this paper is drawn from the publicly available publication of Event Horizon Telescope collaboration ⁵. The data that support the plots within this paper and other findings of this study can be found at https://github.com/XueXiao-Physics/Axion_EHT_2021.

Code Availability The simulation codes used in this study are a modified version of publicly available code IPOLE ^{33,34} (<https://github.com/moscibrodzka/ipole>). The data analysis codes can be found at https://github.com/XueXiao-Physics/Axion_EHT_2021.

Competing Interests Statement The authors declare no competing interests.

References

1. Event Horizon Telescope Collaboration *et al.* First M87 Event Horizon Telescope Results. I. The Shadow of the Supermassive Black Hole. *Astrophys. J. Lett.*, **875**, L1 (2019).
2. Event Horizon Telescope Collaboration *et al.* First M87 Event Horizon Telescope Results. IV. Imaging the Central Supermassive Black Hole. *Astrophys. J. Lett.*, **875**, L4 (2019).
3. Event Horizon Telescope Collaboration *et al.* First M87 Event Horizon Telescope Results. VI. The Shadow and Mass of the Central Black Hole. *Astrophys. J. Lett.*, **875**, L6 (2019).
4. Event Horizon Telescope Collaboration *et al.* First M87 Event Horizon Telescope Results. V. Physical Origin of the Asymmetric Ring. *Astrophys. J. Lett.*, **875**, L5 (2019).
5. Event Horizon Telescope Collaboration *et al.* First m87 event horizon telescope results. VII. polarization of the ring. *Astrophys. J. Lett.*, **910**, L12 (2021).
6. Event Horizon Telescope Collaboration *et al.* First m87 event horizon telescope results. VIII. magnetic field structure near the event horizon. *Astrophys. J. Lett.*, **910**, L13 (2021).
7. Peccei, R. D. & Quinn, H. R. CP Conservation in the Presence of Instantons. *Phys. Rev. Lett.*, **38**, 1440-1443 (1977).
8. Peccei, R. D. & Quinn, H. R. Constraints Imposed by CP Conservation in the Presence of Instantons. *Phys. Rev. D*, **16**, 1791-1797 (1977).
9. Weinberg, S. A New Light Boson? *Phys. Rev. Lett.*, **40**, 223-226 (1978).

10. Wilczek, F. Problem of Strong P and T Invariance in the Presence of Instantons. *Phys. Rev. Lett.*, **40**, 279-282 (1978).
11. Arvanitaki, A., Dimopoulos, S., Dubovsky, S., Kaloper, N. & March-Russell, J. String Axiverse. *Phys. Rev. D*, **81**, 123530 (2010).
12. Preskill, J., Wise, M. B. & Wilczek, F. Cosmology of the Invisible Axion. *Phys. Lett. B*, **120**, 127-132 (1983).
13. Abbott, L. F. & Sikivie, P. A Cosmological Bound on the Invisible Axion. *Phys. Lett. B*, **120**, 133-136 (1983).
14. Dine, M. & Fischler, W. The Not So Harmless Axion. *Phys. Lett. B*, **120**, 137-141 (1983).
15. Chen, Y., Shu, J., Xue, X., Yuan, Q. & Zhao, Y. Probing Axions with Event Horizon Telescope Polarimetric Measurements. *Phys. Rev. Lett.*, **124**, 061102 (2020).
16. Penrose, R. & Floyd, R. M. Extraction of rotational energy from a black hole. *Nature*, **229**, 177-179 (1971).
17. Zel'Dovich, Y. B. Generation of Waves by a Rotating Body. *J. Exp. Theor. Phys. Lett.*, **14**, 180-181 (1971).
18. Press, W. H. & Teukolsky, S. A. Floating Orbits, Superradiant Scattering and the Black-hole Bomb. *Nature*, **238**, 211-212 (1972).
19. Carroll, S. M., Field, G. B. & Jackiw, R. Limits on a Lorentz and Parity Violating Modification of Electrodynamics. *Phys. Rev. D*, **41**, 1231 (1990).
20. Harari, D. & Sikivie, P. Effects of a Nambu-Goldstone boson on the polarization of radio galaxies and the cosmic microwave background. *Phys. Lett. B*, **289**, 67-72 (1992).
21. Yoshino, H. & Kodama, H. Bosenova collapse of axion cloud around a rotating black hole. *Prog. Theor. Phys.*, **128**, 153-190 (2012).
22. Yoshino, H. & Kodama, H. Gravitational radiation from an axion cloud around a black hole: Superradiant phase. *PTEP*, **2014**, 043E02 (2014).
23. Yoshino, H. & Kodama, H. The bosenova and axiverse. *Class. Quant. Grav.*, **32**, 214001 (2015).
24. Baryakhtar, M., Galanis, M., Lasenby, R. & Simon, O. Black hole superradiance of self-interacting scalar fields. *Phys. Rev. D*, **103**, 095019 (2021).
25. Arvanitaki, A. & Dubovsky, S. Exploring the String Axiverse with Precision Black Hole Physics. *Phys. Rev. D*, **83**, 044026 (2011).

26. Dolan, S. R. Instability of the massive Klein-Gordon field on the Kerr spacetime. *Phys. Rev. D*, **76**, 084001 (2007).
27. Schwarz, D. J., Goswami, J. & Basu, A. Geometric optics in the presence of axionlike particles in curved spacetime. *Phys. Rev. D*, **103**, L081306 (2021).
28. Pu, H.-Y. & Broderick, A. E. Probing the innermost accretion flow geometry of Sgr A* with Event Horizon Telescope. *Astrophys. J.*, **863**, 148 (2018).
29. Igumenshchev, I. V., Narayan, R. & Abramowicz, M. A. Three-dimensional mhd simulations of radiatively inefficient accretion flows. *Astrophys. J.*, **592**, 1042-1059 (2003).
30. Narayan, R., Igumenshchev, I. V. & Abramowicz, M. A. Magnetically arrested disk: an energetically efficient accretion flow. *Publ. Astron. Soc. Jap.*, **55**, L69 (2003).
31. McKinney, J. C., Tchekhovskoy, A. & Blandford, R. D. General Relativistic Magnetohydrodynamic Simulations of Magnetically Choked Accretion Flows around Black Holes. *Mon. Not. Roy. Astron. Soc.*, **423**, 3083 (2012).
32. Tchekhovskoy, A. Launching of Active Galactic Nuclei Jets. *Astrophysics and Space Science Library*, **414**, 45 (2015).
33. Moscibrodzka, M. & Gammie, C. F. ipole – semi-analytic scheme for relativistic polarized radiative transport. *Mon. Not. Roy. Astron. Soc.*, **475**, 43-54 (2018).
34. Noble, S. C., Leung, P. K., Gammie, C. F. & Book, L. G. Simulating the Emission and Outflows from Accretion Disks. *Class. Quant. Grav.*, **24**, S259-S274 (2007).
35. Tamburini, F., Thidé, B. & Valle, M. D. Measurement of the spin of the M87 black hole from its observed twisted light. *Mon. Not. Roy. Astron. Soc.*, **492**, L22-L27 (2020).
36. Feng, J. & Wu, Q. Constraint on the black-hole spin of M87 from the accretion-jet model. *Mon. Not. Roy. Astron. Soc.*, **470**, 612 (2017).
37. Davoudiasl, H. & Denton, P. B. Ultralight Boson Dark Matter and Event Horizon Telescope Observations of M87*. *Phys. Rev. Lett.*, **123**, 021102 (2019).
38. Anastassopoulos, V. *et al.* New CAST Limit on the Axion-Photon Interaction. *Nature Phys.*, **13**, 584-590 (2017).
39. Payez, A. *et al.* Revisiting the SN1987A gamma-ray limit on ultralight axion-like particles. *J. Cosmol. Astropart. Phys.*, **02**, 006 (2015).
40. Dessert, C., Foster, J. W. & Safdi, B. R. X-ray Searches for Axions from Super Star Clusters. *Phys. Rev. Lett.*, **125**, 261102 (2020).
41. Marsh, M. C. D. *et al.* A New Bound on Axion-Like Particles. *J. Cosmol. Astropart. Phys.*, **12**, 036 (2017).

42. Reynolds, C. S. *et al.* Astrophysical Limits on Very Light Axion-like Particles from Chandra Grating Spectroscopy of NGC 1275. *Astrophys. J.*, **890**, 59 (2020).
43. Kaplan, D. E. & Rattazzi, R. Large field excursions and approximate discrete symmetries from a clockwork axion. *Phys. Rev. D*, **93**, 085007 (2016).
44. Farina, M., Pappadopulo, D., Rompineve, F. & Tesi, A. The photo-philic QCD axion. *J. High Energy Phys.*, **01**, 095 (2017).
45. Raymond, A. W. *et al.* Evaluation of New Submillimeter VLBI Sites for the Event Horizon Telescope. *Astrophys. J. Supp.*, **253**, 5 (2021).
46. Damour, T., Deruelle, N. & Ruffini, R. On Quantum Resonances in Stationary Geometries. *Lett. Nuovo Cim.*, **15**, 257-262 (1976).
47. Zouros, T. J. M. & Eardley, D. M. Instabilities of massive scalar perturbations of a rotating black hole. *Annals Phys.*, **118**, 139-155 (1979).
48. Detweiler, S. L. Klein-Gordon equation and rotating black holes. *Phys. Rev. D*, **22**, 2323-2326 (1980).
49. Strafuss, M. J. & Khanna, G. Massive scalar field instability in Kerr spacetime. *Phys. Rev. D*, **71**, 024034 (2005).
50. Brito, R., Cardoso, V. & Pani, P. Superradiance: New Frontiers in Black Hole Physics. *Lect. Notes Phys.*, **906**, 1-237 (2015).
51. Cruz-Ororio, A. *et al.* State-of-the-art Energetic and Morphological Modelling of the Launching Site of the M87 Jet. *Nat. Astron.*, in press (2021).
52. Amorim, A. *et al.* Scalar field effects on the orbit of S2 star. *Mon. Not. R. Astron. Soc.*, **489**, 4606-4621 (2019).
53. Arvanitaki, A., Baryakhtar, M. & Huang, X. Discovering the QCD Axion with Black Holes and Gravitational Waves. *Phys. Rev. D*, **91**, 084011 (2015).
54. Brito, R., Cardoso, V. & Pani, P. Black holes as particle detectors: evolution of superradiant instabilities. *Class. Quant. Grav.*, **32**, 134001 (2015).
55. Stott, M. J. Ultralight Bosonic Field Mass Bounds from Astrophysical Black Hole Spin. *Arxiv Preprint*, arXiv:2009.07206 (2020).
56. Ünal, C., Pacucci, F. & Loeb, A. Properties of ultralight bosons from heavy quasar spins via superradiance. *J. Cosmol. Astropart. Phys.*, **05**, 007 (2021).
57. Omiya, H., Takahashi, T. & Tanaka, T. Renormalization group analysis of superradiant growth of self-interacting axion cloud. *PTEP*, **2021**, 043E02 (2021).

58. Narayan, R., Kato, S. & Honma, F. Global structure and dynamics of advection-dominated accretion flows around black holes. *Astrophys. J.*, **476**, 49 (1997).
59. Yuan, F. & Narayan, R. Hot Accretion Flows Around Black Holes. *Ann. Rev. Astron. Astrophys.*, **52**, 529-588 (2014).
60. Prieto, M. A., Fernandez-Ontiveros, J. A., Markoff, S., Espada, D. & Gonzalez-Martin, O. The central parsecs of M87: jet emission and an elusive accretion disc. *Mon. Not. Roy. Astron. Soc.*, **457**, 3801-3816 (2016).
61. Trippe, S. Polarization and Polarimetry. *J. Kor. Astron. Soc.*, **47**, 15-39 (2014).
62. Plascencia, A. D. & Urbano, A. Black hole superradiance and polarization-dependent bending of light. *J. Cosmol. Astropart. Phys.*, **04**, 059 (2018).
63. Ivanov, M. M. *et al.* Constraining the photon coupling of ultra-light dark-matter axion-like particles by polarization variations of parsec-scale jets in active galaxies. *J. Cosmol. Astropart. Phys.*, **02**, 059 (2019).
64. Fujita, T., Tazaki, R. & Toma, K. Hunting Axion Dark Matter with Protoplanetary Disk Polarimetry. *Phys. Rev. Lett.*, **122**, 191101 (2019).
65. Liu, T., Smoot, G. & Zhao, Y. Detecting axionlike dark matter with linearly polarized pulsar light. *Phys. Rev. D*, **101**, 063012 (2020).
66. Fedderke, M. A., Graham, P. W. & Rajendran, S. Axion Dark Matter Detection with CMB Polarization. *Phys. Rev. D*, **100**, 015040 (2019).
67. Caputo, A. *et al.* Constraints on millicharged dark matter and axionlike particles from timing of radio waves. *Phys. Rev. D*, **100**, 063515 (2019).
68. Yuan, G.-W. *et al.* Testing the ALP-photon coupling with polarization measurements of Sagittarius A*. *J. Cosmol. Astropart. Phys.*, **03**, 018 (2021).
69. Johannsen, T. & Psaltis, D. Testing the No-Hair Theorem with Observations in the Electromagnetic Spectrum: II. Black-Hole Images. *Astrophys. J.*, **718**, 446-454 (2010).
70. Gralla, S. E., Holz, D. E. & Wald, R. M. Black Hole Shadows, Photon Rings, and Lensing Rings. *Phys. Rev. D*, **100**, 024018 (2019).
71. Johnson, M. D. *et al.* Universal interferometric signatures of a black hole's photon ring. *Sci. Adv.*, **6**, eaaz1310 (2020).
72. Gralla, S. E. & Lupsasca, A. Lensing by Kerr Black Holes. *Phys. Rev. D*, **101**, 044031 (2020).
73. Jiménez-Rosales, A. *et al.* Relative depolarization of the black hole photon ring in GRMHD models of Sgr A* and M87*. *Mon. Not. Roy. Astron. Soc.*, **503**, 4563-4575 (2021).

74. Marti-Vidal, I., Mus, A., Janssen, M., de Vicente, P. & Gonzalez, J. Polarization calibration techniques for the new-generation VLBI. *Astron. Astrophys.*, **646**, A52 (2021).